



Development of a homogenous disposal MOX powder for plutonium immobilisation

Jack Rolfe¹ · Colin Boxall¹ · Richard Wilbraham¹ · Dave Goddard² · Hayley Green³

Received: 16 April 2025 / Accepted: 12 June 2025 / Published online: 18 June 2025
© The Author(s) 2025

Abstract

Disposal MOX (dMOX), a sintered mixed U, Pu, oxide containing a neutron poison, such as Gd, is currently under consideration for immobilisation of the UK's civil plutonium inventory. Prior to deployment, it is important to understand how material homogeneity impacts overall behavior of the wastefrom. Therefore, while using Ce as a non-active Pu surrogate, this study outlines a methodology for the production of a homogenous dMOX precursor powder to be subsequently sintered to a homogenous dMOX pellet. The powder was produced via reverse-strike oxalate co-precipitation of a Ce(III), Gd(III), and photochemically conditioned U(IV) precursor solution, which was then calcined to a mixed oxide in a 5% H_2 /95% N_2 reaction atmosphere. SEM–EDX and PXRD analysis revealed the oxalate and mixed oxide to be fully homogeneous, with no evidence of segregated phases. TGA decomposition found the oxalate to decompose in several distinct stages, agreeing with established literature, resulting in a fully homogenous mixed oxide powder.

Introduction

The United Kingdom (UK) currently possesses the world's largest stockpile of civil Pu, $\approx 140\text{te}$, accumulated from its hydrometallurgical reprocessing of spent nuclear fuel (SNF) [1]. Prolonged, indefinite storage of this material in its existing state, a separated PuO_2 powder, presents a risk of nuclear proliferation and a security burden for future generations to manage. Therefore, it is imperative that this material is promptly disposed of in a manner that places it “beyond reach” [2]. Following a government decision in January 2025, it was announced that the UK's Pu inventory is to be rendered inaccessible via immobilisation within a suitable ceramic wastefrom, followed by permanent disposition to a Geological Disposal Facility (GDF) [3]. One potential avenue to Pu immobilisation is as a disposal mixed oxide (dMOX) ceramic. This is envisioned to comprise of a sintered pellet of a minor fraction of PuO_2 in

solid-solution with UO_2 , similar in design to MOX nuclear fuel [4–6]. Immobilising Pu through a MOX-type ceramic is advantageous for several key reasons. Firstly, both UO_2 and PuO_2 adopt the cubic fluorite crystal structure (space group $\text{Fm-}3\text{m}$), which is regarded to be extremely durable in high-radiation environments [7]. Additionally, both materials have attractive material properties, such as high melting points (2827 °C for UO_2 [8] and 2744 °C for PuO_2 [9]) and comparably high densities (10.97 gcm^{-3} for UO_2 [10] and 11.50 gcm^{-3} for PuO_2 [11]). Importantly, it is also suggested that dMOX could be manufactured through pre-established industrial processes, similar to those currently utilised for MOX fuel fabrication [5, 12]. This is desirable when considering the relative industrial immaturity of other potential Pu immobilisation options, such as the Hot Isostatic Pressing (HIP) of titanate ceramics [13].

As the dMOX wastefrom will contain relatively high levels of fissile Pu, there is a clear risk of an unwanted neutron chain reaction occurring upon groundwater ingress in a geological repository—necessitating the need for criticality control. This could be achieved by doping the wastefrom with a suitable neutron absorbing element such as Gd_2O_3 or HfO_2 . Both materials have large neutron absorption cross-sections and are compatible with the crystalline structure of PuO_2 [4]. Moreover, Gd_2O_3 has been shown to be easily incorporable into the UO_2 matrix while simultaneously reducing its corrosion susceptibility, improving pellet resistance to

✉ Jack Rolfe
j.rolfe1@lancaster.ac.uk

¹ Engineering Department, Lancaster University,
Lancaster LA1 4YW, UK

² United Kingdom National Nuclear Laboratory (UKNNL),
Springfields, Preston PR4 0XJ, UK

³ Sellafield Ltd., Seascale CA20 1PG, UK

dissolution [14, 15]. Understanding how the level of homogeneity throughout the final sintered pellet can influence wastefrom behaviour is important in the advancement of the dMOX concept. Homogenous mixed oxide powders, which can be subsequently sintered to homogenous pellets, can be produced through wet chemical approaches such as oxalate co-precipitation [16]. In a recent study, the fabrication of a homogenous (U, Th, Gd) O_{2-x} dMOX pellet was explored, with the precursor powder produced via direct-strike oxalate co-precipitation of a U(VI) containing solution [6]. It was reported that the intermediate oxalate product was partially inhomogeneous, with the inhomogeneity perpetuating through to the final sintered pellet. Uranium recovery during fabrication was also found to be slightly lower than targeted, attributed to the low, unideal pH of the oxalic acid solution used during the initial precipitation step. It is also possible that uranium recovery could have been additionally impacted by the redox state of the uranium ion, as U(VI) oxalates are reported to be partially soluble at room temperature [17]. Horlait et al. [18] used reverse-strike oxalate co-precipitation to produce $Th_{1-x}Ln(III)_xO_{2-x/2}$ mixed oxides, successfully reporting the final powder to be single phase fluorite despite 27 mol% Gd doping. Zsbaka et al. [19] also attempted to produce $Th_{1-x}Gd_xO_{2-x/2}$ through direct-strike oxalate co-precipitation, instead observing two segregated Th and Gd rich phases. With these previous studies in mind, it is hypothesised that the partial separate oxalate formation observed in previous studies could be resolved by application of a reverse-strike mixing method.

Therefore, in this study, while employing Ce as a non-active Pu surrogate, a method for the production of a homogenous (U, Ce, Gd) O_{2-x} powder is detailed via co-precipitation and calcination of a mixed U, Ce, Gd oxalate. In contrast to the work above, a photochemical reduction step was used to convert a UO_2^{2+} containing precursor solution to U(IV) [20], ensuring the precipitation of an insoluble U(IV) oxalate. A reverse-strike mixing technique was also employed. Notably, as U(IV) acts as a reducing agent capable of reducing Pu(IV) to Pu(III), the photochemical reduction of a mixed U(VI)/Pu(IV)/Gd(III) solution to the more precipitable U(IV) would yield the production of Pu(III) [21], subsequently precipitating as an insoluble Pu(III) oxalate. This opposes conventional Pu finishing processes, which primarily focus on the precipitation of Pu(IV) oxalate. In this context, Ce(III) serves as a suitable surrogate for Pu.

Methods and materials

Unless otherwise specified, all materials were AnalaR grade or higher and obtained from Thermo Scientific Chemicals (UK) or Sigma-Aldrich (UK). All water was ultrapure

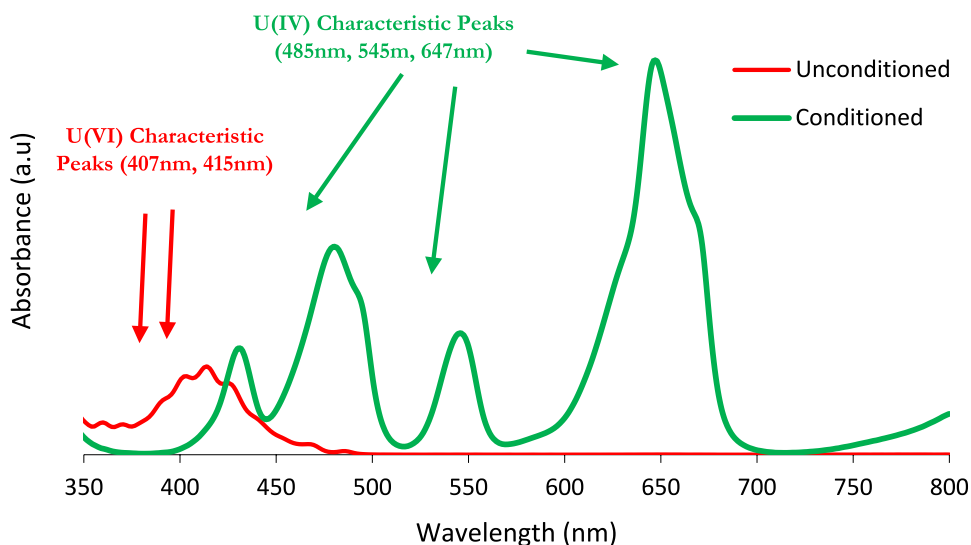
doubly de-ionised water supplied by a Direct-Q 3 UV Millipore water purification system (Millipore, UK).

The synthesis of the homogenous oxide powders was completed in four distinct stages: photochemical conditioning of a U(VI) precursor solution, precipitation of a mixed-metal oxalate powder, powder recovery via overnight vacuum filtration, and calcination to a U(IV) mixed-metal oxide. The target composition of the final mixed oxide was $U_{0.89}Ce_{0.1}Gd_{0.01}O_{2-x}$, representing a realistic 10 mol% Pu loading and Gd to Pu ratio of 1:10 [6].

Regarding the photochemical conditioning, $UO_2(NO_3)_2 \cdot 6H_2O$ (ABSCO Ltd., UK) was firstly dissolved in 1 mol dm^{-3} HNO_3 to produce a 205 mmol dm^{-3} U(VI) solution, to which 1 mol dm^{-3} isopropyl-alcohol (IPA) and 50 mmol dm^{-3} N_2H_4 was added. The IPA was added as a sacrificial reductant, with the N_2H_4 added to scavenge any photochemically or radiolytically generated HNO_2 , therefore preventing unwanted reoxidation to U(VI) [20]. The solution was then passed through a continuous flow-through photoreactor illuminated with 407 nm LZC-70UB00-00U8 LED emitters with a spectral half-width of $\pm 10 \text{ nm}$ (LED Engine Ltd., UK). The total illuminated residence time was 10 min. Upon illumination a distinct colour change was observed, with the solution transitioning from pale yellow to dark green. Successful conditioning of the metal ion was confirmed through UV-Vis spectrophotometry in a Shimadzu UV-2600 UV-Vis Spectrophotometer (Shimadzu UK Ltd., UK), shown in Fig. 1. Following conditioning, 23 mmol dm^{-3} Ce(III) and 2.3 mmol dm^{-3} Gd(III) were added in the form of $Ce(NO_3)_3 \cdot 6H_2O$ and $Gd(NO_3)_3 \cdot 6H_2O$.

10 cm^3 aliquots of the mixed-metal ion solution were then added dropwise to sample tubes containing 10 cm^3 of 0.6 mol dm^{-3} oxalic acid in a Radleys Carousel Reaction Station (Radley & Co Ltd., UK) in a reverse-strike fashion. This was completed at room temperature. The oxalate ligand to metal ion ratio was 2.6:1, allowing for an approximate 0.6 mol oxalate excess. Upon contact, a pale-green oxalate precipitate was instantly formed. The solution was then continuously stirred for 2 h at 400 rotations per minute. The precipitate was recovered via overnight vacuum filtration through a sintered glass disc funnel filter (Fisher Scientific, UK). The recovered mixed-metal oxalate was calcined to a mixed oxide powder in a STA7200 TGA/DSC (Hitachi, Japan) in a Pt pan to $900 \text{ }^\circ\text{C}$ under a 5% H_2 /95% N_2 (99.9% purity) reaction atmosphere, with a heating rate of $10 \text{ }^\circ\text{C min}^{-1}$. All gas flows were 0.1 dm^3 per minute. The morphology of both the mixed-metal oxalates and oxides was examined via Scanning Electron Microscopy (SEM) in a TESCAN AMBER BrightBeam UHR-SEM (TESCAN, Czechia), equipped with an Oxford Instruments Ultim Max 40 Energy Dispersive X-Ray (EDX) Analyser (Oxford instruments, UK) allowing semi-quantitative assessment of metal ion spatial distributions. Powder X-Ray Diffraction

Fig. 1 UV–Vis spectra of solution before and after photochemical conditioning



(PXRD) patterns were collected in a Rigaku Smartlab X-ray diffractometer (Rigaku Europe SE, Germany) mounted in parallel beam configuration with a Cu X-ray target.

Oxalate scans were taken from 10° to 50° with a step size of 0.01° , with oxide scans taken from 25° to 100° with a step size of 0.1° , due to the material being significantly more crystalline. PXRD samples were prepared by sealing a small amount of powder (≈ 5 mg) on an ABS plastic tray with Kapton tape. All spectra were baseline subtracted and smoothed using the Savitsky-Golay approach. Reference spectra were obtained from the Inorganic Crystal Structure Database (ICSD). Lattice parameters were calculated at 2θ angles $> 65^\circ$ via Bragg's law. These calculated lattice parameters were then refined via the extrapolation of the Nelson–Riley function, subsequently reducing systematic error.

Results and discussion

SEM images of the precipitated mixed-metal oxalate and calcined oxide powders can be seen in Fig. 2. The oxalate powder appeared to be extremely fine, with an average particle size of $\approx 5 \mu\text{m}$. It exhibited a square-platelet morphology, which is consistent with previous observations on An(IV) oxalate powders [22, 23]. This morphology was also found in the calcined oxide powder. EDX analysis revealed the powder to contain an even distribution of both U, Ce, and Gd, with no detectable presence of inhomogeneity, implying the creation of homogenous mixed-metal oxide powder.

The TGA decomposition trace of the mixed oxalate when calcined under a reducing $5\% \text{H}_2/95\% \text{N}_2$ atmosphere is shown in Fig. 3. Complete decomposition had occurred by $\approx 600^\circ \text{C}$ agreeing with previous observations on the decomposition of dMOX oxalates [6].

As can be seen, the oxalate lost mass in several steps. The first three of these can be attributed to the removal of absorbed water—U(IV) oxalate hexahydrate molecules have been reported to dehydrate in three stages when calcined under inert atmospheres, the first occurring between 27 and 97°C , the second between 97 and 137°C and third 137 – 234°C [24]. These stages broadly correlate with the first three DTG peaks, albeit with a slight shift to higher temperatures. The first mass loss was calculated as $\approx 14.3\%$, strongly resembling the theoretical value for the removal of 4 mol of water (14.2%). The second loss of $\approx 3.6\%$ also agreed with the theoretical value for the removal of an additional mole of water (3.6%). The final dehydration related mass loss of $\approx 4.9\%$ was slightly higher than the theoretical loss from one final mole of water, but is still in general agreement. Above temperatures of 284°C , decomposition of the dehydrated oxalate compound to a mixed oxide initiated. This mass loss of $\approx 25.9\%$ was slightly lower than the theoretical calculated value of 27.5%. It is likely that this discrepancy is due to a small overlap between the final dehydration mass loss and the initiation of oxalate decomposition, also explaining why the measured value for the former was marginally greater than the theoretical value. Overall, the total measured mass loss of $\approx 50.3\%$ is in good agreement with the theoretical value of 50.5%. The small deviation of $\approx 0.2\%$ is likely due to the deposition of elemental carbon on the powder surface, resulting from the disproportionation of CO via the Boudouard equilibrium, which has been reported to occur when calcining An oxalates under both inert and reducing conditions [25, 26].

Importantly, each DTA peak appeared to be distinct without any additional features, supporting the observations from the SEM–EDX analysis above and PXRD below that a single phase mixed U, Ce, Gd oxalate, which subsequently decomposed into a homogeneous mixed oxide, was formed.

Fig. 2 **a** SEM image of mixed-metal oxalate powder, **b** SEM image of mixed-metal oxide powder, **c** U ion distribution in mixed-metal oxide powder, **d** Ce ion distribution in mixed-metal oxide powder, **e** Gd ion distribution in mixed-metal oxide powder

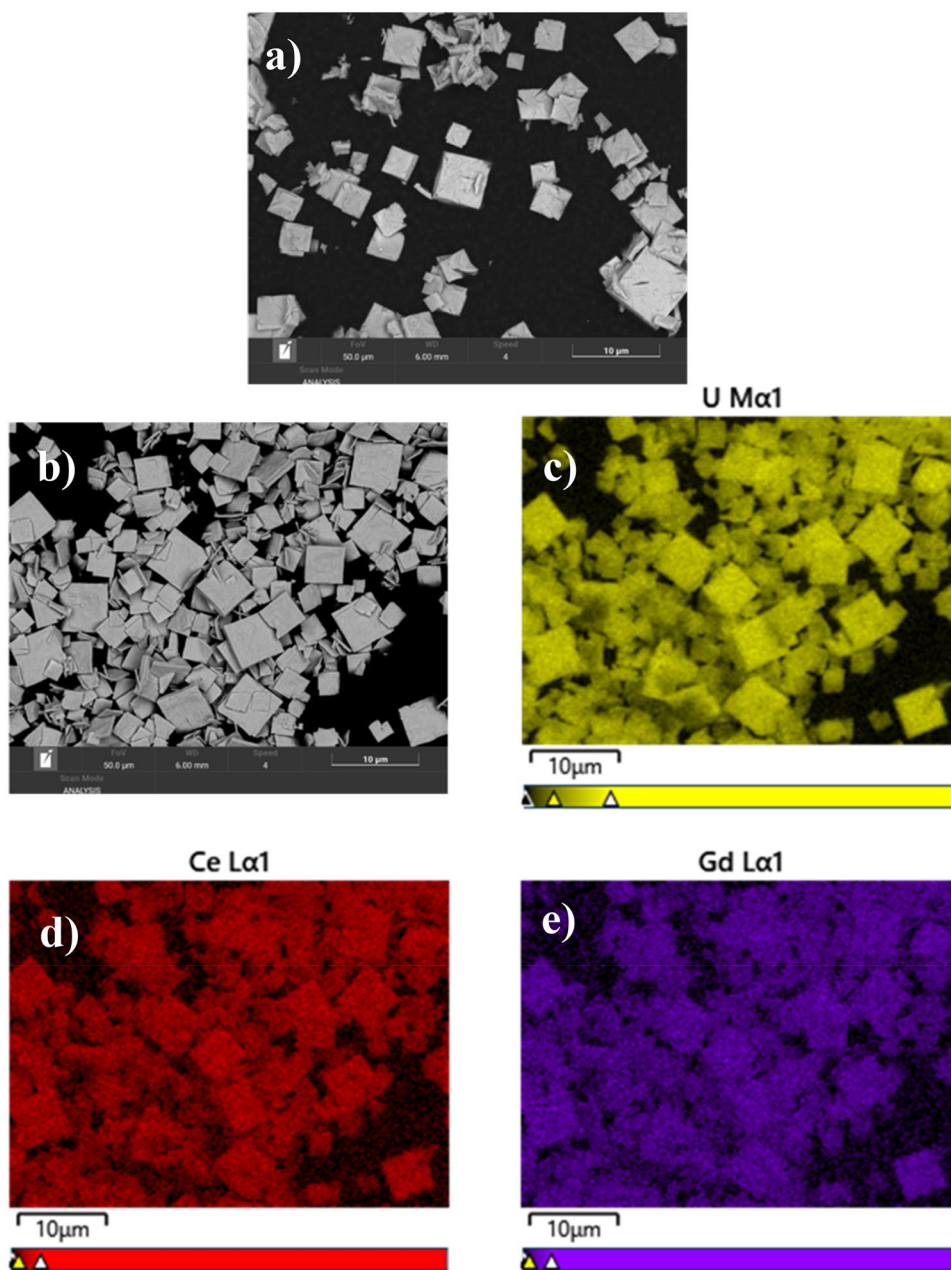
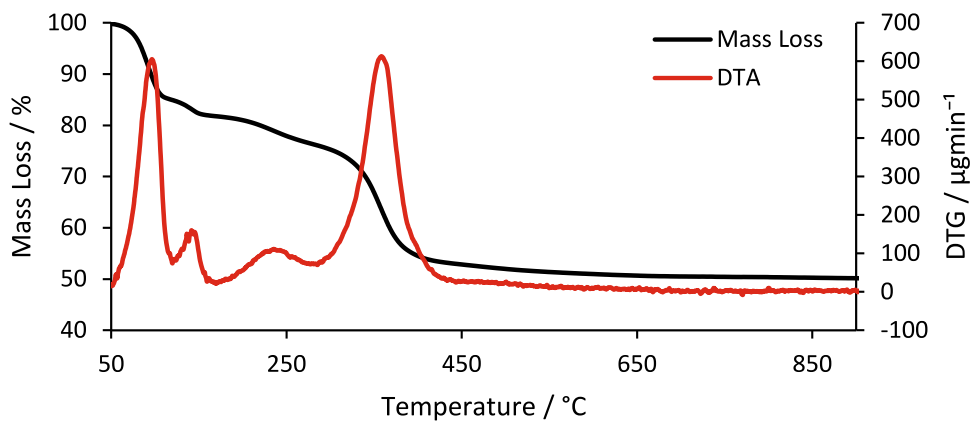


Fig. 3 TGA decomposition of mixed-metal oxalate under 5% $H_2/95\% N_2$ atmosphere



The PXRD spectra of both the mixed oxalate and calcined mixed oxide powder are shown in Fig. 4.

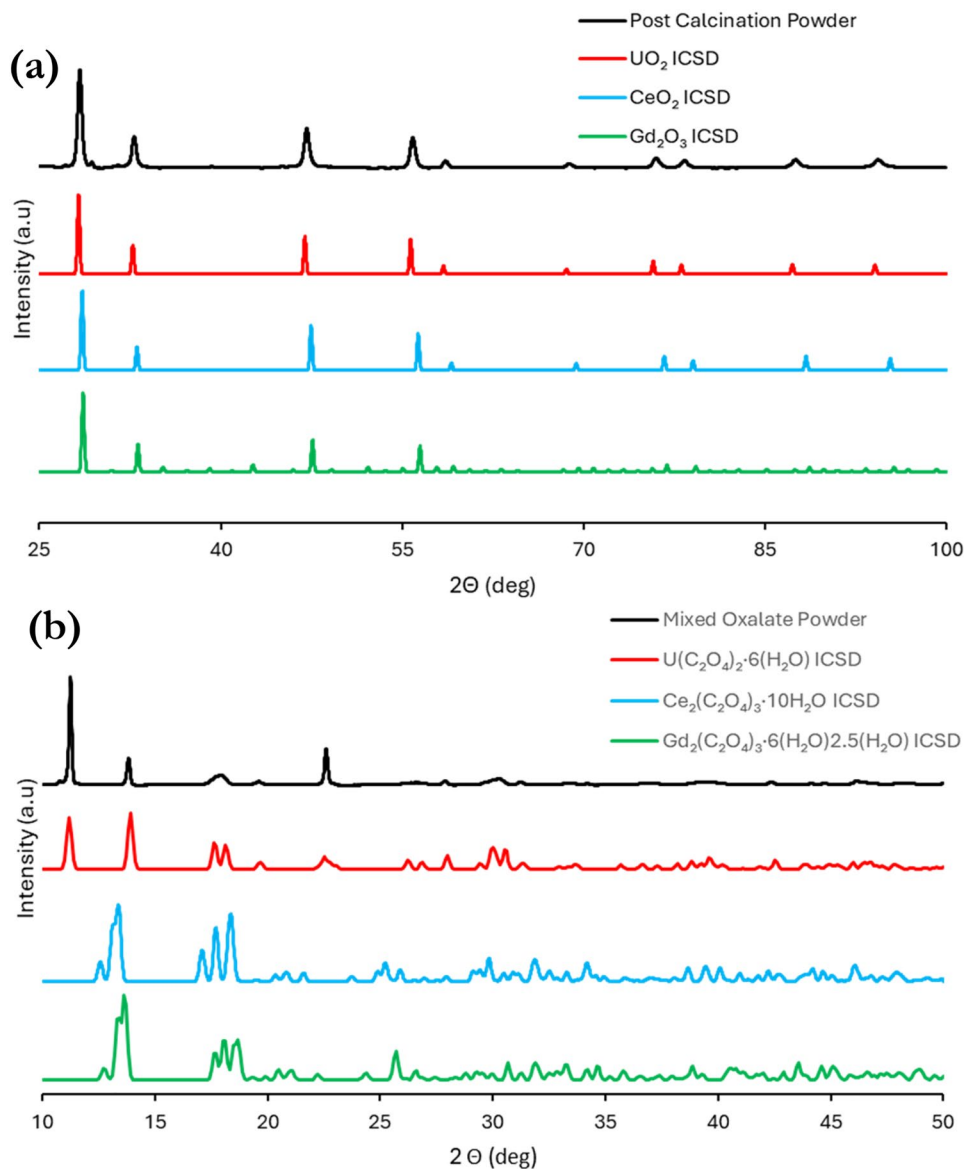
The oxalate powder shared good similarity to the ICSD reference spectrum for monoclinic $U(C_2O_4)_2(H_2O)_6$, implying full incorporation of the Ce and Gd ions into the U oxalate structure, with charge neutrality ensured through the protonation of water to H_3O^+ . There was no evidence to suggest that $N_2H_5^+$ was incorporated as a charge balancing cation, which has been shown to instead promote the formation of a hexagonal structured mixed oxalate [27].

The calcined mixed oxide powder spectrum appeared to strongly resemble the ICSD reference spectrum for cubic UO_2 . Considering the lack of both CeO_2 and Gd_2O_3 minor peaks, this observation is further evidence to suggest a single phase homogenous mixed-metal oxide powder was synthesised, with the relevant Ce and Gd ions fully incorporated

into the UO_2 parent matrix and structure. The oxide pattern exhibited an additional minor additional peak at 28.85° , arising from the ABS plastic holder in which the powders were mounted.

At higher reflections, the mixed oxide exhibited a shift to higher angles versus the ICSD reference for stoichiometric UO_2 , indicative of a contraction in lattice parameter—subsequently calculated as 5.4568 \AA . The theoretical lattice parameter, if assuming Ce as being incorporated in its tetravalent Ce(IV) state, was found to be 5.46436 \AA . The theoretical lattice parameter was calculated by applying Vegard's law to CeO_2 (5.4124 \AA) [28] and $U_{0.988}Gd_{0.112}O_{2-x}$ (5.4693 \AA), with the lattice parameter of the latter found through the relationship proposed by Baena et al. [29]. This theoretical lattice parameter is greater than that measured, implying the presence of additional factors contributing to

Fig. 4 **a** PXRD spectrum of mixed oxalate powder, **b** PXRD spectrum of mixed oxide powder



lattice contraction, such as the production of oxygen vacancies and/or U(V) generation as charge compensation mechanisms [14]. However, it is also likely that Ce is present in its trivalent Ce(III) state, due to both the presence of Ce(III) in the initial mixed oxalate and the reducing calcination atmosphere. Despite this, Ce(III) presence would result in a larger theoretical lattice parameter, due to Ce(III) possessing a larger ionic radii than Ce(IV), resulting in greater disparity between the measured and theoretical value [30]. Therefore, the presence of some Ce(IV) content cannot be ruled out, as mass spectrometry of the off-gases generated during the TGA experiments of Fig. 3 revealed that oxygen was released during the decomposition of the oxalate (data not shown)—and this may have oxidised some of the larger ionic radii Ce(III) to smaller Ce(IV). Further characterisation is required, through techniques such as X-Ray Photoelectron Spectroscopy (XPS), in order to determine the Ce valence state and thus explore this hypothesis. This, coupled with additional TGA studies, could also help to underpin the quantity of U(V), and therefore the stoichiometry, within the material.

Conclusion

A route to a homogenous mixed U, Ce, Gd oxide powder has been developed as a precursor for a sintered homogenous surrogate dMOX pellet. By applying a photochemical conditioning step to ensure the subsequent precipitation of a U(IV) oxalate and a reverse-strike mixing method, a mixed oxalate powder was produced that exhibited no sign of metal ion inhomogeneity, which carried through to the calcined mixed oxide powder. PXRD analysis revealed that the lattice parameter of the mixed oxide was smaller than anticipated, likely resulting from charge compensation mechanisms. The powders prepared from this study can be used in future trials to understand how important metal ion homogeneity is in the behaviour of the final sintered wasteform.

Acknowledgments All work was conducted in Lancaster University's UTGARD Laboratory, a National Nuclear User Facility supported by the UK Research & Innovation's (UKRI) Engineering & Physical Sciences Research Council (EPSRC) (award EP/T011416/1). The authors would also like to thank the Nuclear Decommissioning Authority for funding this work through the UKRI GREEN Centre for Doctoral Training.

Author contributions J. Rolfe: Investigation, formal analysis, visualisation, methodology, writing - original draft. C. Boxall: Conceptualisation, funding acquisition, project administration, supervision, writing - review & editing. R. Wilbraham: Investigation, supervision. D. Goddard: Supervision, writing - review & editing. H. Green: Supervision, writing - review & editing.

Funding J. Rolfe is funded by the Nuclear Decommissioning Authority and the UKRI GREEN Centre for Doctoral Training (EP/S022295/1).

Data availability The datasets generated during and/or analysed during the current study are available from the corresponding author on reasonable request.

Declarations

Ethical approval On behalf of all authors, the corresponding author states that there is no conflict of interest.

Open Access This article is licensed under a Creative Commons Attribution 4.0 International License, which permits use, sharing, adaptation, distribution and reproduction in any medium or format, as long as you give appropriate credit to the original author(s) and the source, provide a link to the Creative Commons licence, and indicate if changes were made. The images or other third party material in this article are included in the article's Creative Commons licence, unless indicated otherwise in a credit line to the material. If material is not included in the article's Creative Commons licence and your intended use is not permitted by statutory regulation or exceeds the permitted use, you will need to obtain permission directly from the copyright holder. To view a copy of this licence, visit <http://creativecommons.org/licenses/by/4.0/>.

References

1. Cadman L., Goater, A., *Managing the UK plutonium stockpile*. PN513, Houses of Parliament, 2016.
2. *Progress on plutonium consolidation, storage and disposition*. 2019, Nuclear decommissioning authority: https://assets.publishing.service.gov.uk/media/5c9e3e0140f0b625e1cbd851/Progress_on_Plutonium.pdf. Accessed 24 April 2025
3. *Plutonium disposition strategy*. 2025, UK Government: <https://questions-statements.parliament.uk/written-statements/detail/2025-01-24/hlws384> Accessed 24 April 2025
4. J. Kang et al., Storage MOX: A third way for plutonium disposal? *Sci. Glob. Secur.* **10**(2), 85–101 (2002). <https://doi.org/10.1080/08929880213803>
5. A. Macfarlane et al., Plutonium disposal, the third way. *Bullet. Atom. Sci.* **57**(3), 53–57 (2001). <https://doi.org/10.2968/057003015>
6. M.R. Cole et al., A disposal-MOX concept for plutonium disposition. *Mater. Adv.* **5**(16), 6416–6425 (2024). <https://doi.org/10.1039/d4ma00420e>
7. W.J. Weber et al., Radiation effects in crystalline ceramics for the immobilization of high-level nuclear waste and plutonium. *J. Mater. Res.* **13**(2), 1434–1484 (1998). <https://doi.org/10.1557/JMR.1998.0205>
8. L. Burakovsky et al., Ambient melting behavior of stoichiometric uranium oxides. *Front. Nucl. Eng.* (2024). <https://doi.org/10.3389/fnuen.2023.1215418>
9. F. De Bruyker et al., Reassessing the melting temperature of PuO₂. *Mater. Today* **13**(11), 52–55 (2010). [https://doi.org/10.1016/S1369-7021\(10\)70204-2](https://doi.org/10.1016/S1369-7021(10)70204-2)
10. G. Leinders et al., Accurate lattice parameter measurements of stoichiometric uranium dioxide. *J. Nucl. Mater.* **249**, 135–142 (2015). <https://doi.org/10.1016/j.jnucmat.2015.01.029>
11. M.P. Wilkerson et al., Structural properties, thicknesses, and qualities of plutonium oxide thin films prepared by polymer assisted deposition. *Surf. Sci.* **701**, 121696 (2020). <https://doi.org/10.1016/j.susc.2020.121696>
12. C.L. Corkhill et al., Demonstration of industrially-fabricated plutonium disposition MOX. *J. Nucl. Mater.* **603**, 155477 (2025). <https://doi.org/10.1016/j.jnucmat.2024.155477>

13. L.R. Blackburn et al., Hot isostatically pressed Zirconalite Waste-forms for actinide immobilisation. *IOP Conf. Ser.: Mater. Sci. Eng.* **818**, 012010 (2020). <https://doi.org/10.1088/1757-899X/818/1/012010>
14. N. Liu et al., Influence of Gd doping on the structure and electrochemical behaviour of UO_2 . *Electrochim. Acta* **247**, 496–504 (2017). <https://doi.org/10.1016/j.electacta.2017.07.006>
15. A. Casella, B. Hanson, W. Miller, The effect of fuel chemistry on UO_2 dissolution. *J. Nucl. Mater.* **476**, 45–55 (2016). <https://doi.org/10.1016/j.jnucmat.2016.04.025>
16. M.J. Sarsfield, in *Reprocessing and Recycling of Spent Nuclear Fuel*, ed. by Robin Taylor (Woodhead Publishing, Cambridge, 2015), p. 325–351. <https://doi.org/10.1016/B978-1-78242-212-9.00013-7>
17. F. Abraham et al., Actinide oxalates, solid state structures and applications. *Coord. Chem. Rev.* **266–267**, 28–68 (2014). <https://doi.org/10.1016/j.ccr.2013.08.036>
18. D. Horlait et al., Synthesis and characterisation of $\text{Th}_{1-x}\text{Ln}_x\text{O}_{2-x/2}$ mixed oxides. *Mater. Res. Bull.* **47**(12), 4017–4025 (2012). <https://doi.org/10.1016/j.materresbull.2012.08.068>
19. P. Zsabka et al., Synthesis of gadolinium-doped thorium dioxide via a wet chemical route: Limitations of the co-precipitation method. *J. Nucl. Mater.* **489**, 211–221 (2017). <https://doi.org/10.1016/j.jnucmat.2017.03.052>
20. M.A. Bromley et al., The rapid photochemical reduction of U(VI) at high uranium concentrations relevant to spent nuclear fuel recycle processes. *Prog. Nucl. Energy* **164**, 104853 (2023). <https://doi.org/10.1016/j.pnucene.2023.104853>
21. G.L. DePoorter et al., Photochemically produced U(IV) as a reductant for Pu(IV) and applications in nuclear fuel reprocessing. *Nucl. Technol.* **43**(2), 132–135 (1979). <https://doi.org/10.13182/NT79-A16304>
22. J. Martinez et al., From uranium (IV) oxalate to sintered UO_2 : Consequences of the powders' thermal history on the microstructure. *J. Eur. Ceram. Soc.* **35**(16), 4535–4546 (2015). <https://doi.org/10.1016/j.jeurceramsoc.2015.07.010>
23. N. Hingant et al., Preparation, sintering and leaching of optimized uranium thorium dioxides. *J. Nucl. Mater.* **385**(2), 400–406 (2009). <https://doi.org/10.1016/j.jnucmat.2008.12.011>
24. G.K. Çılgı, H. Cetişli, R. Donat, Thermal and kinetic analysis of uranium salts. Part III. Uranium(IV) oxalate hydrates. *J. Therm. Anal. Calorimet.* **115**, 2007–2020 (2013). <https://doi.org/10.1007/s10973-013-3341-7>
25. L. De Almeida et al., New insights on the thermal decomposition of lanthanide(III) and actinide(III) oxalates: From neodymium and cerium to plutonium. *J. Inorg. Chem.* **31**, 4986–4999 (2012). <https://doi.org/10.1002/ejic.201200469>
26. Y. Ziouane et al., Speciation of residual carbon containing in UO_2 . *J. Solid State Chem.* **244**, 45–51 (2016). <https://doi.org/10.1016/j.jssc.2016.09.003>
27. E. Brackx et al., Structural study of $(\text{N}_2\text{H}_5, \text{H})_{2.9}\text{U}_{1.1}\text{Ce}_{0.9}(\text{C}_2\text{O}_4)_5 \cdot 10\text{H}_2\text{O}$ from a conventional X-ray diffraction diagram obtained on a powder synthesized by a fast vortex process. *J. Solid State Chem.* **221**, 166–172 (2015). <https://doi.org/10.1016/j.jssc.2014.09.030>
28. M. Wołczyr, L. Kepinski, Rietveld refinement of the structure of CeOCI formed in Pd/CeO₂ catalyst: Notes on the existence of a stabilized tetragonal phase of La₂O₃ in La-Pd-O system. *J. Solid State Chem.* **99**(2), 409–413 (1992). [https://doi.org/10.1016/0022-4596\(92\)90330-X](https://doi.org/10.1016/0022-4596(92)90330-X)
29. A. Baena et al., Lattice contraction and lattice deformation of UO_2 and ThO_2 doped with Gd_2O_3 . *J. Nucl. Mater.* **467**(1), 135–143 (2015). <https://doi.org/10.1016/j.jnucmat.2015.09.018>
30. J.M. Elorrieta et al., Pre- and post- oxidation Raman analysis of (U,Ce)₂O₃ oxides. *J. Nucl. Mater.* **508**, 116–122 (2018). <https://doi.org/10.1016/j.jnucmat.2018.05.042>

Publisher's Note Springer Nature remains neutral with regard to jurisdictional claims in published maps and institutional affiliations.